Electronic Supplementary Information

# Solvent-modulated proton-coupled electron transfer in an iridium complex with an ESIPT ligand

*Siin Kim,*[a,b] *Jungkweon Choi,*[a,b,] *Dae Won Cho,*[c] *Mina Ahn,*[d] *Seunghwan Eom,*[a,b] *Jungmin Kim,*[a,b] *Kyung-Ryang Wee,*[d,*] *Hyotcherl Ihee* [a,b,*]

a. Department of Chemistry and KI for the BioCentury, Korea Advanced Institute of Science and Technology (KAIST), Daejeon 34141, Republic of Korea

b. Center for Advanced Reaction Dynamics, Institute for Basic Science, Daejeon 34141, Republic of Korea

c. Department of Advanced Materials Chemistry, Korea University, Sejong Campus, Sejong 30019, Korea

d. Department of Chemistry and Institute of Natural Science, Daegu University, Gyeongsan 38453, Republic of Korea

* Corresponding authors: Kyung-Ryang Wee and Hyotcherl Ihee

E-mail: krwee@daegu.ac.kr and hyotcherl.ihee@kaist.ac.kr

**Experimental**

**Synthesis and characterization:** All of the synthesis procedures were performed under a dry argon condition. Reagents and solvents were obtained from commercial suppliers and used without further purification. Deuterated solvent for NMR experiments was obtained from Merck or Cambridge Isotope Lab. Inc. Silica gel column chromatography was performed with silica gel 60 G (230–400 mesh ASTM, Merck Co.). The synthesized compounds were characterized by $^1$H-NMR and elemental analysis. The $^1$H spectra were recorded on a Bruker500 spectrometer operating at 500 MHz, and all proton chemical shifts were measured relative to internal residual chloroform (99.9 % $CDCl_3$), acetone (99.9 % $(CD_3)_2CO$) or dimethyl sulfoxide (99.8 % $(CD_3)_2SO$) from the lock solvent. The elemental analyses (C, H, N, O) were performed using a Thermo Fisher Scientific Flash 2000 series analyzer. Electrospray ionization (ESI) mass spectra were measured using a Xevo TQ-S micro (Waters$^{TM}$) instrument. The dichloro-bridged iridium dimer complex, **[Ir(dfppy)$_2$(μ-Cl)]$_2$**, was prepared based on the previously published method.[1] As shown in Scheme S1, the final Ir(III) complexes (**Ir-PIPN** and **Ir-PIPP-H**), containing 2-(1-phenyl-1H-imidazo[4,5-f][1,10]phenanthrolin-2-yl)naphthalen-2-ol and 2-(1-phenyl-1H-imidazo[4,5-f][1,10]phenanthrolin-2-yl)phenol as ancillary ligands (PIPP-H and PIPN), were successfully synthesized and the detail synthesis procedure is described in Scheme S1.

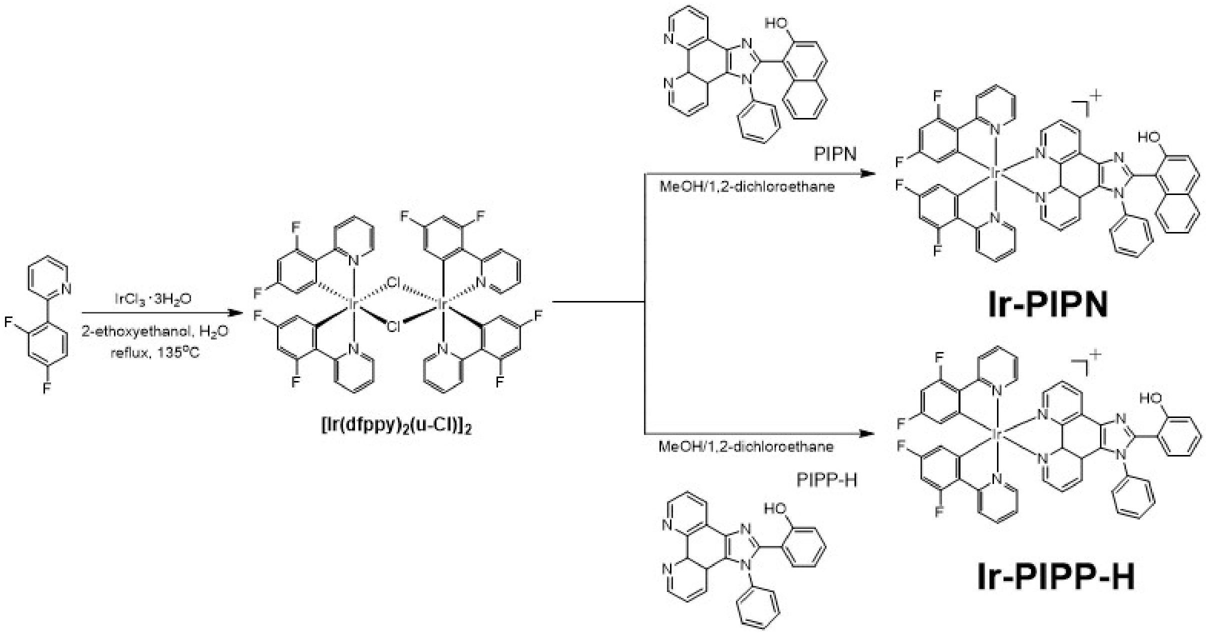


**Scheme S1.** Synthesis routes of two Ir (III) complexes (Ir-PIPN and Ir-PIPP-H).

**General synthesis of two ESIPT Ir(III) complexes (Ir-PIPN and Ir-PIPP-H):** A solution of 0.04 mmol of $[Ir(dfppy)_2(\mu\text{-}Cl)]_2$ and 0.10 mmol of PIPN and PIPP-H in MeOH/1,2-dichloroethane (v/v = 2:1, 12 mL) was refluxed at 85 ºC under argon for 2 hours. After the solution was cooled to room temperature, a saturated aqueous solution of $NH_4PF_6$ (5 mL) was added to the resulting solution and the solution was stirred overnight. The reaction mixture was extracted with DCM and water using a separating funnel. The separated organic layer was dried over anhydrous $MgSO_4$ and then filtered off. The solvent was removed under reduced pressure, and the final products were obtained by recrystallization from *n*-hexane/$CH_2Cl_2$.

**Ir-PIPN.** *Iridium (III) bis(2-(2,4-difluorophenyl)pyridinato-N,C$^{2'}$)(1-(1-phenyl-1H-imidazo [4,5-f][1,10]phenanthrolin-2-yl)naphthalen-2-ol)* Yield: 30 %, green powder. $^1$H-NMR (500 MHz, $(CD_3)_2SO$, ppm) δ 10.30 (d, 1 H), 8.50 (d, 1 H), 8.35 (t, 3 H), 8.10 (m, 1 H), 8.03 (t, 2 H), 7.75 (t, 1 H), 7.62 (m, 1 H), 7.42 (m, 1 H), 7.10 (m, 4 H), 5.75 (m, 2 H)., Anal. Found (Calc) for $C_{51}H_{30}F_4IrN_6O^+$: C, 60.59 (60.47); H, 2.99 (3.18); N, 8.31 (8.30); O, 1.58 (1.58). ESI-MS Calcd for $[C51H30F4IrN6O]^+$: 1011.2 m/z, Found: 1012 m/z.

**Ir-PIPP-H.** *Iridium (III) bis(2-(2,4-difluorophenyl)pyridinato-N,C$^{2'}$)(2-(1-phenyl-1H-imidazo [4,5-f][1,10]phenanthrolin-2-yl)phenol)* Yield: 45 %, orange powder. $^1$H-NMR (500 MHz, $CDCl_3$, ppm) δ 9.22 (d, 1 H), 8.28 (t, 3 H), 8.15 (d, 1 H), 7.96 (d, 1 H), 7.88 (m, 2 H), 7.81 (t, 1 H), 7.70 (m, 4 H), 7.58 (d, 1 H), 7.52 (m, 3 H), 7.32 (d, 1H), 7.27 (t, 1 H), 7.09 (m, 2 H), 6.90 (t, 1H), 6.83 (d, 1H), 6.58 (m, 3H), 5.77 (d, 2H)., Anal. Found (Calc) for $C_{47}H_{28}F_4IrN_6O^+$: C, 58.74 (58.62); H, 2.94 (3.14); N, 8.75 (8.73); O, 1.66 (1.66). ESI-MS Calcd for $[C47H28F4IrN6O]^+$: 961.2 m/z, Found: 962 m/z.

**Spectroscopic measurements:** We used a UV-visible spectrophotometer (Shimadzu, UV-2550) and a fluorometer (PerkinElmer, LS-55) to measure absorption and emission spectra, respectively. The fluorescence lifetime of Ir-PIPN was measured with a time-correlated single-photon counting (TCSPC) technique (HORIBA, Fluorolog3). The sample was excited with the 374 nm pulse from a diode laser. The femtosecond time-resolved absorption spectra were collected with a pump–probe transient absorption spectroscopy system. The output pulses at a wavelength of 800 nm from a Ti:sapphire amplified laser (Coherent Legend Elite) were split into the pump and probe beams. On the pump arm, the laser pulses of 800 nm were converted into the pump pulses of the wavelength of 350 nm using an optical parametric amplifier (Spectra Physics, OPAS prime). A white-light continuum pulse, which was generated by focusing the residual of the fundamental light onto a 1 mm path length quartz cell containing water, was used as a probe beam. The white light was directed to the sample cell with an optical path of 2.0 mm and detected with a CCD detector installed in the absorption spectroscopy system after the controlled optical delay. The pump pulse was chopped by a mechanical chopper synchronized to one-half of the laser repetition rate, resulting in a pair of spectra with and without the pump pulse, from which the absorption change induced by the pump pulse was estimated.

**Density Functional Theory (DFT) and time-dependent DFT (TDDFT) calculations:** TDDFT calculations were implemented by Q-Chem 5.0[2] suite of ab initio quantum chemistry programs, using CAM (Handy's Coulomb-attenuating range-separated functional)-B3LYP[3] with Grimme's D3 dispersion correction[4]. The iridium was modeled with the LANL2DZ basis set with the effective core potentials[5–7]. The other atoms were modeled with the standard double-ζ quality 6-31G** basis set[8]. Eigenstates of the time-dependent hamiltonians were constructed based on configuration interaction singles (CIS), which is equivalent to the Tamm-Dancoff Approximation (TDA)[9].

The optimized structure of the $T_1$ state of Ir-PIPN is shown in Figure S10. The determined dihedral angle ($\theta$(CCCN)) between the proton donating and proton accepting groups is 24.0°. The structure of the PIPN ligand in the optimized Ir-PIPN structure is similar to the optimized structure of cis-keto (*cis*-K*) of PIPN, which has a dihedral angle of 39.7°.[10] A study for PIPN reported that PIPN shows two rotational isomers for keto form, namely, cis-keto and per-keto (*per*-K*) with a dihedral angle of 39.7° and 106.6°, respectively, according to DFT and TDDFT calculations.[10] In contrast to the free PIPN, the PIPN ligand in Ir-PIPN exists as a cis-keto with a dihedral angle of 24.0° in Ir-PIPN.

**Singular value decomposition (SVD) analysis:** We applied the SVD analysis to our experimental TA data of Ir-PIPN in DCM and in DCM/EtOH (20/80) in the $\lambda$ range of 400 – 700 nm. From the experimental TA spectra measured at various time delays, we can build an $n_\lambda \times n_t$ matrix **A**, where $n_\lambda$ is the number of $\lambda$ points in the TA spectrum at a given time-delay point (255 wavelength points) and $n_t$ is the number of time-delay points (70 and 95 time delay points in the wavelength range from 400 nm to 700 nm for Ir-PIPN in DCM and in DCM/EtOH (20/80), respectively). Then, the matrix **A** can be decomposed while satisfying the relationship of $\mathbf{A} = \mathbf{USV}^T$, where **U** is an $n_\lambda \times n_t$ matrix whose columns are called left singular vectors (lSVs) (i.e. time-independent $\lambda$ spectra) of **A**, **V** is an $n_t \times n_t$ matrix whose columns are called right singular vectors (rSVs) (i.e. amplitude changes of **U** as time evolves) of **A**, and **S** is an $n_t \times n_t$ diagonal matrix whose diagonal elements are called singular values of **A** and can possess only non-negative values. The matrices **U** and **V** have the properties of $\mathbf{U}^T\mathbf{U} = \mathbf{I}_{nt}$ and $\mathbf{V}^T\mathbf{V} = \mathbf{I}_{nt}$, respectively, where $\mathbf{I}_{nt}$ is the identity matrix. Since the diagonal elements (i.e. singular values) of **S**, which represent the weight of left singular vectors in **U**, are ordered so that $s_1 \geq s_2 \geq \cdots \geq s_n \geq 0$, (both left and right) singular vectors on more left are supposed to have larger contributions to the constructed experimental data. In this manner, we can extract the time-independent transient absorption components from the lSVs and the time evolution of their amplitudes from the rSVs. The former, when combined together, can give information on the TA spectra of distinct transient species, while the latter contains information on the population dynamics of the transient species.

From the singular values and autocorrelations of the corresponding singular vectors, the first $n_p$ singular vectors enough to represent our experimental data can be determined because the contribution of each singular vector (lSV or rSV) to the data is proportional to its corresponding singular value and the autocorrelation of **U** or **V** matrix can serve as a good measure of the signal-to-noise ratio of the singular vectors (in this study, two and three significant singular components for the data of Ir-PIPN in DCM and in DCM/EtOH (20/80), respectively). In other words, the contribution from the $(n_p + 1)_{\text{th}}$ singular vectors and beyond becomes negligible. The SVD analysis results are shown in Figures S9 (Ir-PIPN in DCM) and S17 (Ir-PIPN in DCM/EtOH (20/80)).

To extract kinetic information, as many rSVs as $n_p$ multiplied by singular values were fit by a sum of multiple exponentials sharing common relaxation times as follows:

$$s_o V_{o,fit} = c_o + \sum_{i=1}^{m} A_{i,o} e^{-t/t_i} \quad \text{(Eqn. S1)}$$

where $s_o$ is $o$th singular value, $V_{o,fit}(t)$ are the calculated $o$th rSVs to fit $V_o(t)$, which are $o$th rSVs from SVD, $t$ are time delays, $c_o$ is a constant for the $V_{o,fit}(t)$ offset, $m$ is the number of exponential functions, $A_{i,o}$ is the amplitude for $i$th exponential of $V_{o,fit}(t)$, $t_i$ is the $i$th sharing relaxation time. The $V_{o,fit}(t)$ values are optimized by minimizing the discrepancy between $V_o(t)$ and $V_{o,fit}(t)$. The discrepancy is quantified by the test function (TF), which is the sum of every residual between $V_{o,fit}(t)$ and $o$th rSVs, $V_o(t)$, as shown in the following equation:

$$TF = \sum_{t}^{n_t} \sum_{o=1}^{n_p} \left| s_o V_o(t) - s_o V_{o,fit}(t) \right| \quad \text{(Eqn. S2)}$$

To find an appropriate number of exponentials, we performed the fitting by changing the number of exponentials. For the data from Ir-PIPN in DCM, the first two rSVs were simultaneously fitted with a single exponential function with a shared relaxation time, 10.8 ± 2.1 ps. $V_{o,fit}(t)$ with more than one exponential function could fit $V_o(t)$, but some exponential time constants show no meaningful difference, indicating that they were overfitted. For the data from Ir-PIPN in DCM/EtOH (20/80), the first three rSVs were simultaneously fitted with a sum of bi-exponential functions with shared relaxation times, 1.2 ± 0.1 ps, 7.4 ± 0.5 ps. $V_{o,fit}(t)$ with less than two exponential functions could not provide a satisfactory fit to $V_o(t)$. $V_{o,fit}(t)$ with more than two exponential functions could fit $V_o(t)$, but some exponential time constants show no meaningful difference, indicating that they were overfitted.

**Kinetic analysis:** Using the first few singular vectors of significant singular values (that is, $n_p$ principal singular vectors) obtained from the SVD analysis of the experimental data, we performed the kinetic analysis. New matrices, **U'**, **V'**, and **S'**, can be defined by removing non-significant components from **U**, **V**, and **S**, respectively. In other words, **U'** is an $n_\lambda \times n_p$ matrix containing the first $n_p$ left singular vectors of **U**, **V'** is an $n_t \times n_p$ matrix containing the first $n_p$ right singular vectors of **V**, and **S'** is an $n_p \times n_p$ diagonal matrix containing the first $n_p$ singular values of **S**. Here, we represent the time-dependent concentrations of transiently formed intermediate species, which can be calculated from a kinetic model, by a matrix **C**. Then, the matrix **C** can be related to **V'** by using a parameter matrix **P** that satisfies **V'** = **CP**, where **C** is an $n_t \times n_p$ matrix whose columns represent time-dependent concentrations of transiently formed intermediate species and **P** is an $n_p \times n_p$ matrix whose columns contain coefficients for the time-dependent concentrations so that the linear combination of concentrations of the $n_p$ intermediates can form the $n_p$ right singular vectors in **V'** Once **C** is specified by a kinetic model with a certain set of variable kinetic parameters such as rate coefficients, **P** and **C** can be optimized by minimizing the discrepancy between **V'** (from the experiment) and **CP** (from the kinetic theory).

Since **V'** = **CP**, the following relationships hold:

$$\mathbf{A'} = \mathbf{U'S'V'}^{\mathrm{T}} = \mathbf{U'S'}(\mathbf{CP})^{\mathrm{T}} = \mathbf{U'S'P}^{\mathrm{T}}\mathbf{C}^{\mathrm{T}} = (\mathbf{U'S'P}^{\mathrm{T}})\mathbf{C}^{\mathrm{T}} \qquad \text{(Eqn. S3)}$$

where **A'** is an $n_\lambda \times n_t$ matrix that contains the theoretical TA spectrum $\Delta A(\lambda_i,t_j)$ at given $\lambda$ and $t$ values. Theoretical TA spectra calculated by using Eqn. S1 were compared with the experimental TA spectra, and the matrix **P** and **C** were optimized by minimizing the discrepancy (quantified by least-square, LS) between the theoretical and experimental TA spectra using the Minuit[11] package:

$$LS = \sum_{i=1}^{n_\lambda} \sum_{j=1}^{n_t} \{A_{exp}(\lambda_i, t_j) - A_{the}(\lambda_i, t_j)\}^2 \qquad \text{(Eqn. S4)}$$

$\Delta A_{exp}(\lambda_i,t_j)$ and $\Delta A_{the}(\lambda_i,t_j)$ are the experimental and theoretical TA spectrum at a given point of $(\lambda_i,t_j)$, respectively. From Eqn. S1, we can define a matrix **B** as **B** = **U'S'P**$^T$, that is, a linear combination of the $n_p$ left singular vectors in **U'** weighted by their singular values in **S'** with their ratios determined by **P**. Then, the matrix **E**, an $n_t \times n_p$ matrix, contains the $n_p$ time-independent TA spectra directly associated with the $n_p$ intermediate species. Therefore, by optimizing the matrices P and C, we obtain both the time-dependent concentrations (see the optimized **C** for the kinetic model in Figures 3e and 4e) and the time-independent TA spectra of the intermediate species (see the optimized **P** for the kinetic model in Figure 3d and 4d).

For Ir-PIPN in DCM, based on the single exponential time constant obtained from the exponential fitting of rSVs (Figure S9b) and two principal components from SVD analysis results (Figures S9), we tested the sequential kinetic model with one time constant and two intermediates. This kinetic model gave a satisfactory fit between the experimental and the calculated spectra. For Ir-PIPN in DCM/EtOH (20/80), considering the two exponential time constants obtained from the exponentials fitting of rSVs (Figure S17b) and three principal components from SVD analysis results (Figures S17), the sequential kinetic model with two time constants and three intermediates was used. The fit with this kinetic model gave a satisfactory agreement between the experimental and the calculated spectra.

## Reference


1. K. J. Suhr, L. D. Bastatas, Y. Shen, L. A. Mitchell, B. J. Holliday and J. D. Slinker, Enhanced luminance of electrochemical cells with a rationally designed ionic iridium complex and an ionic additive. *ACS Appl. Mater. Interfaces* 2016, ***8***, 8888-8892
2. Shao Y. et al., Advances in molecular quantum chemistry contained in the Q-Chem 4 program package. *Mol. Phys.* 2015, **113**, 184-215.
3. Yanai, T.; Tew, D.; Handy, N., A new hybrid exchange–correlation functional using the Coulomb-attenuating method (CAM-B3LYP). *Chem. Phys. Lett.* 2004, **393**, 51.

4. S. Grimme, J. Antony, S. Ehrlich and H. Krieg, A consistent and accurate ab initio parametrization of density functional dispersion correction (DFT-D) for the 94 elements H-Pu. *J. Chem. Phys.* 2010, **132**, 154104.
5. P. J. Hay and W. R. Wadt, *Ab initio* effective core potentials for molecular calculations. Potentials for K to Au including the outermost core orbitals. *J. Chem. Phys.* 1985, **82**, 299-310.
6. P. J. Hay and W. R. Wadt, *Ab initio* effective core potentials for molecular calculations. Potentials for the transition metal atoms Sc to Hg. *J. Chem. Phys.* 1985, **82**, 270-283.
7. W. R. Wadt and P. J. Hay, *Ab initio* effective core potentials for molecular calculations. Potentials for main group elements Na to Bi. *J. Chem. Phys.* 1985, **82**, 284-298.
8. R. Ditchfield, W. J. Hehre and J. A. Pople, Self-Consistent Molecular-Orbital Methods. IX. An Extended Gaussian-Type Basis for Molecular-Orbital Studies of Organic Molecules. *J. Chem. Phys.* 1971, **54**, 724-728.
9. S. Hirata and M. Head-Gordon, Time-dependent density functional theory within the Tamm–Dancoff approximation. *Phys. Lett.* 1999, **314**, 291-299.
10. J. Choi, D. S. Ahn, S. Y. Gal, D. W. Cho, C. Yang, K. R. Wee and H. Ihee, Sterically Controlled Excited-State Intramolecular Proton Transfer Dynamics in Solution, *J. Phys. Chem. C*, 2019, **123**, 29116-29125.
11. SMART and SAINT; Bruker Analytical X-ray Division: Madison, WI, 2002. (52) Sheldrick, G. M. SHELXTL-PLUS Software Package; Bruker Analytical X-ray Division: Madison, WI, 2002.

**Table S1.** Emission lifetime of Ir complexes in DCM

| | Ir-PIPN | Ir-PIPP-H |
|---|---|---|
| | τ (μs) | τ (μs) |
| With oxygen | 0.35 ± 0.01 | 0.47 ±0.1 |
| Without oxygen | 1.1 ± 0.01 | 1.0 ± 0.1 |

**Table S2.** Time constants determined from the fitting of time profiles monitored at specific wavelengths and the fitting of the rSVs from SVD. Time constants obtained from the latter method are shown in parentheses

| Ir-PIPN | | | Ir-PIPP-H | |
|---|---|---|---|---|
| Solvent | $\tau_1$ | $\tau_2$ | Solvent | $\tau_1$ |
| DCM/EtOH = 100/0 | 6.4 ± 1.1 ps<br>(10.8 ± 2.1 ps) | | DCM/EtOH = 100/0 | 3.7 ± 0.7 ps |
| DCM/EtOH = 20/80 | 1.2 ± 0.1 ps<br>(1.2 ± 0.1 ps) | 6.6 ± 0.5 ps<br>(7.4 ± 0.5 ps) | | |

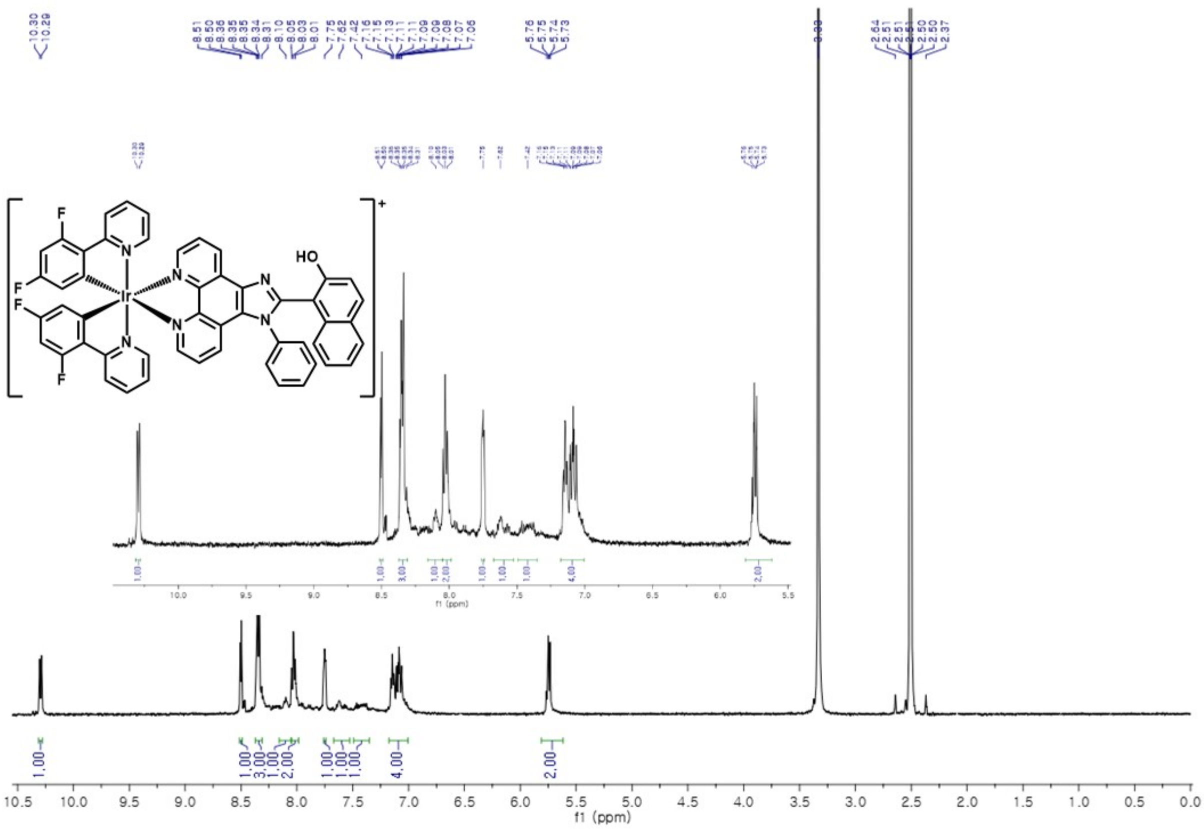

**Figure S1.** $^{1}$H-NMR spectrum of Ir-PIPN in $(CD_3)_2SO$ (500 MHz, 293 K).

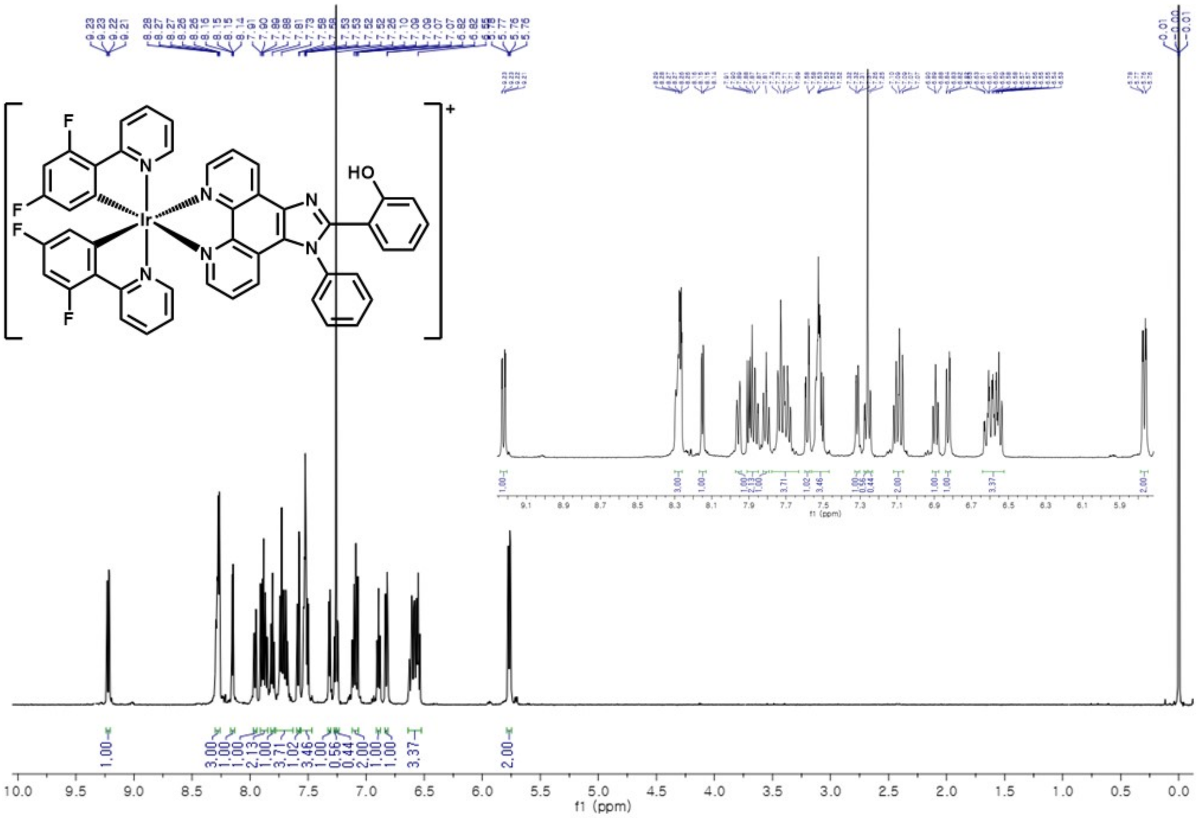

**Figure S2.** $^{1}$H-NMR spectrum of Ir-PIPP-H in $CDCl_3$ (500 MHz, 293 K).

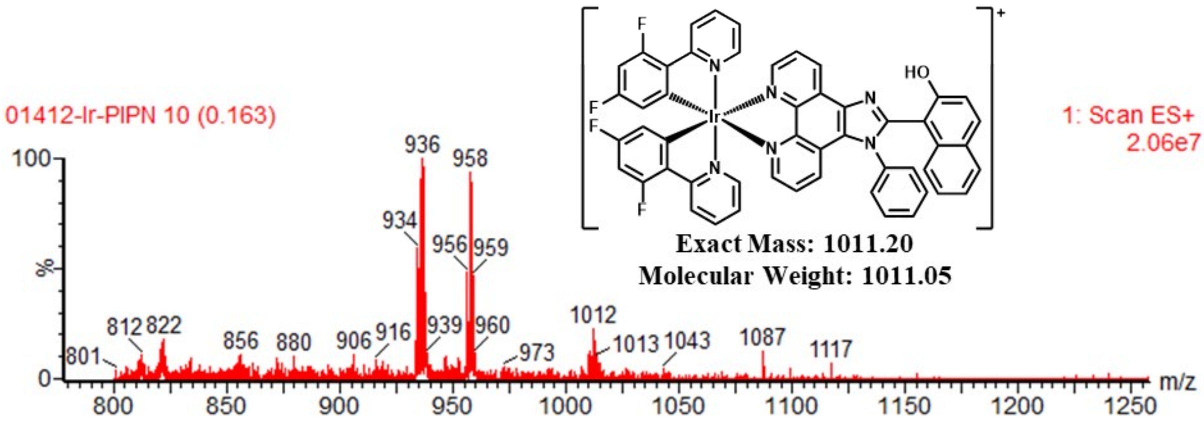


**Figure S3.** Electrospray ionization (ESI) mass spectrum for Ir-PIPN.

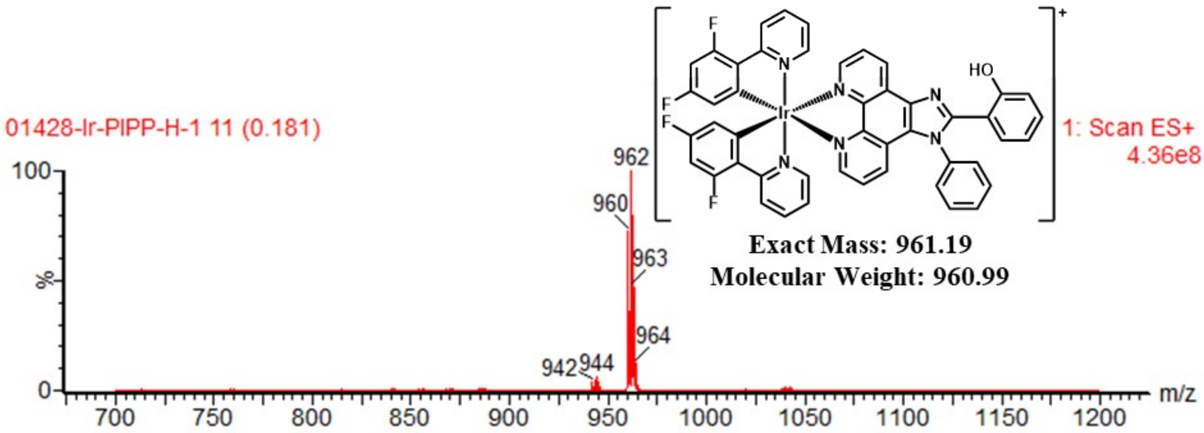


**Figure S4.** Electrospray ionization (ESI) mass spectrum for Ir-PIPP-H.

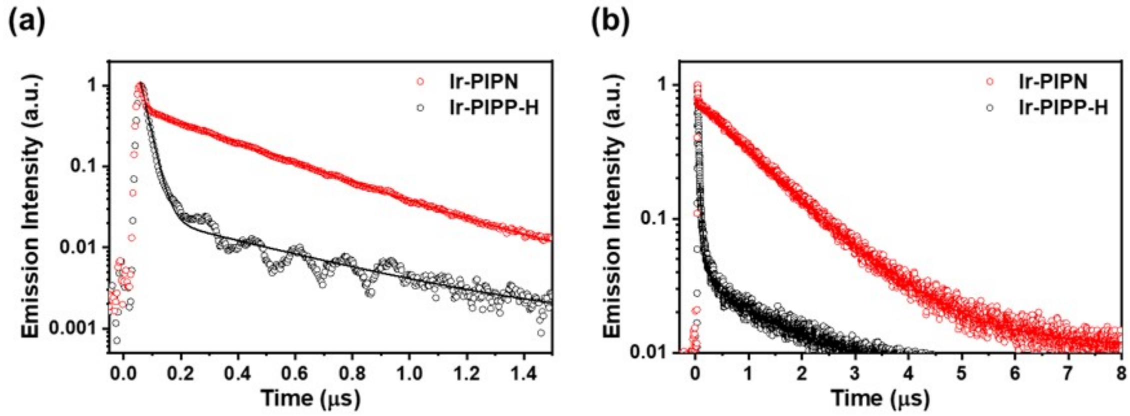


**Figure S5.** Emission decay profiles monitored at 510 nm for Ir-PIPN and Ir-PIPP-H (a) in the presence of oxygen and (b) in the absence of oxygen. The excitation wavelength is 355 nm.

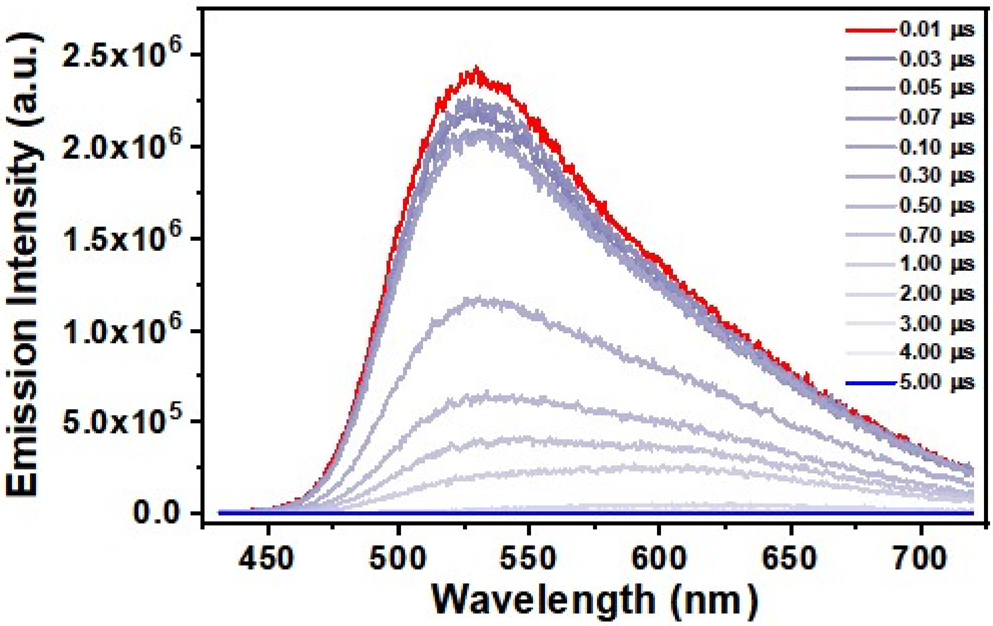


**Figure S6.** Time-resolved emission spectra of Ir-PIPN in DCM. The excitation wavelength is 355 nm.

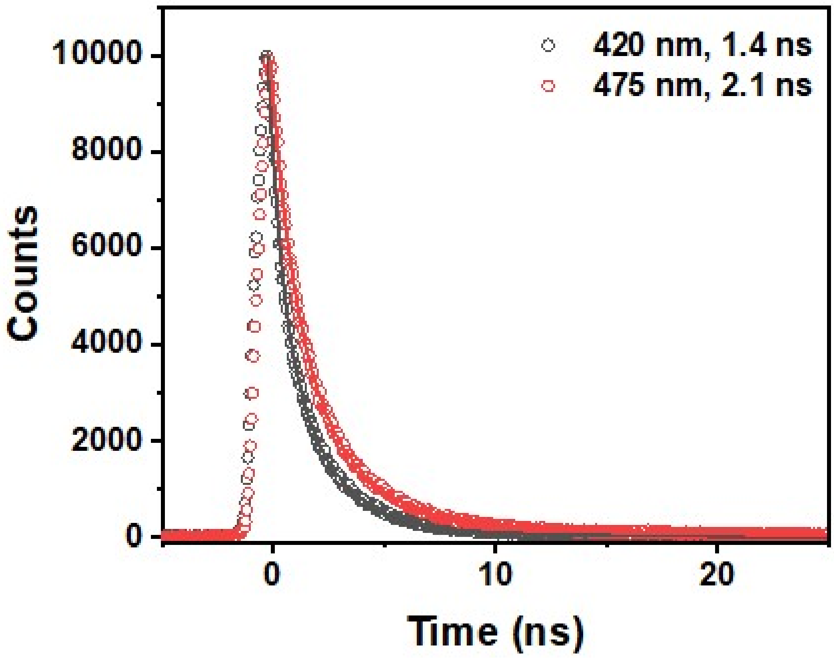


**Figure S7.** TCSPC data (circles) of Ir-PIPN in DCM and their fits (solid lines). The monitored emission wavelengths and the corresponding fluorescence lifetimes are indicated in the legend. The absorbance was adjusted to be less than 0.3 at the excitation wavelength of 374 nm.

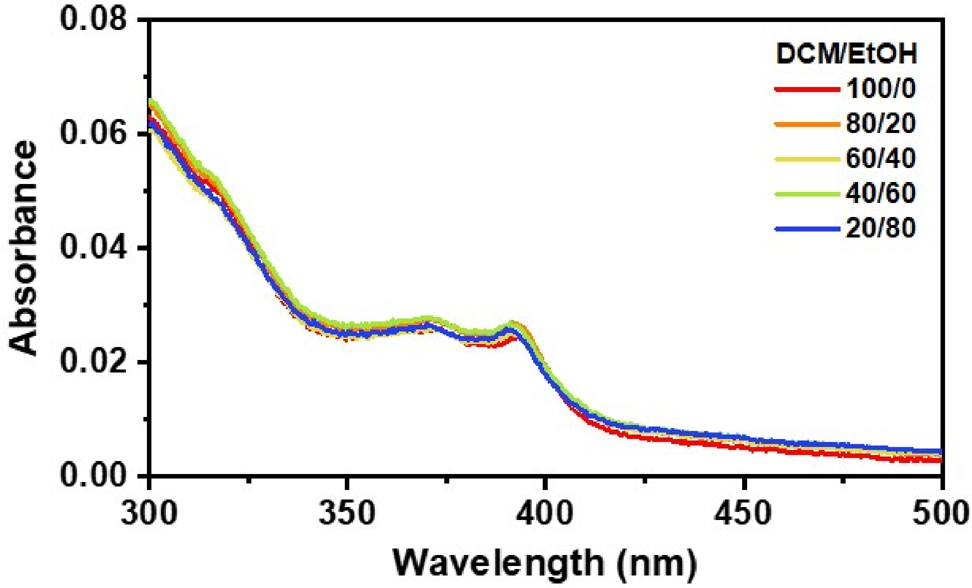


**Figure S8.** The absorption spectra of Ir-PIPN in DCM/EtOH mixtures with various ratios (100/0, 80/20, 60/40, 40/60, and 20/80).

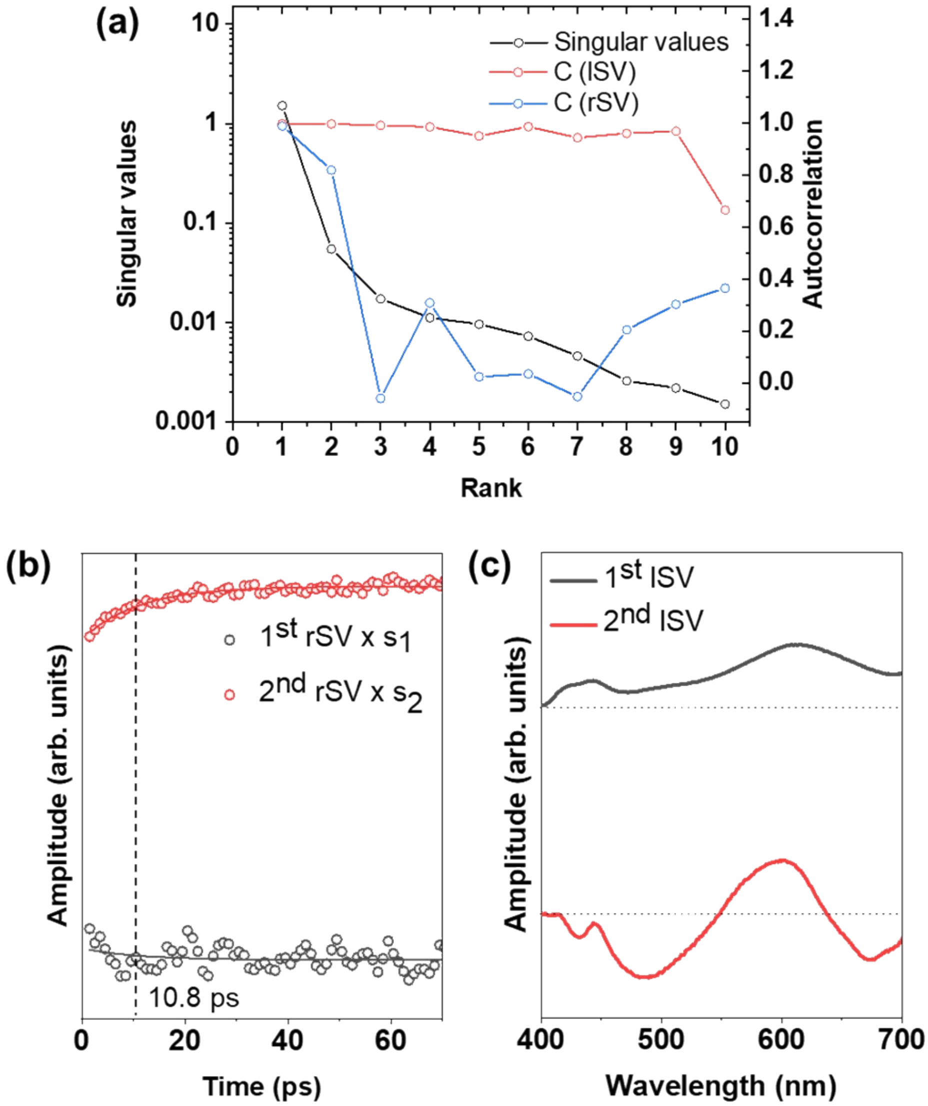


**Figure S9.** (a) The SVD results of Ir-PIPN in DCM. The singular values and the autocorrelation values for left singular vectors (lSVs) and right singular vectors (rSVs) obtained from the SVD analysis of TA experimental data of Ir-PIPN in DCM. The singular values and the autocorrelation values indicate that up to two components contribute significantly to the TA data. (b) The first two rSVs weighted by the corresponding singular values. The solid lines are the fits by a single exponential function sharing one time constant of 10.8 ± 2.1 ps. (c) The first two lSVs.

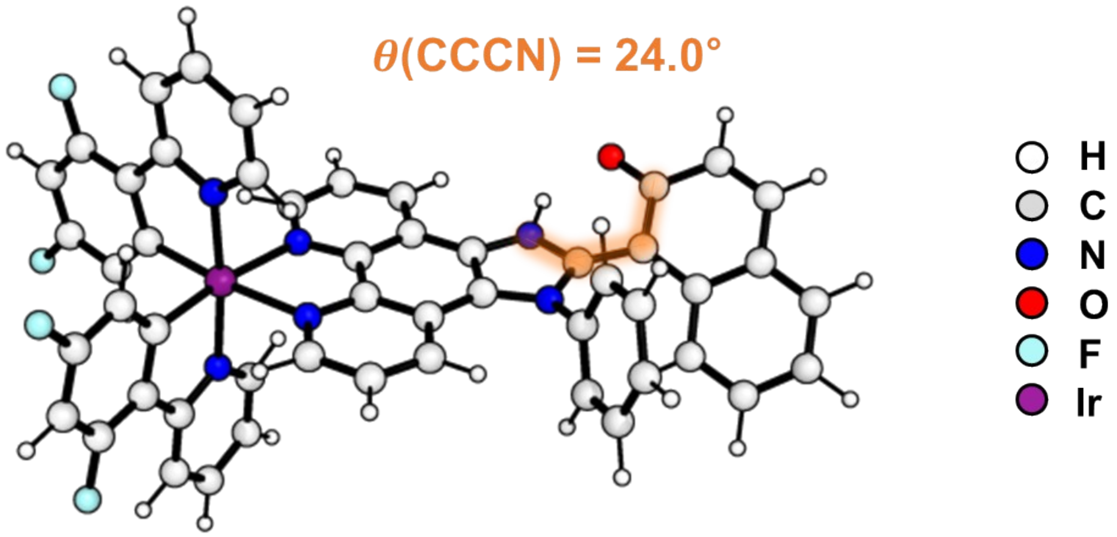


**Figure S10.** The optimized structure of $T_1$ state of Ir-PIPN. The obtained dihedral angle ($\theta$(CCCN), orange) between of the proton donating and proton accepting groups is 24.0°.

| State | Energy | HONTO | LUNTO |
|---|---|---|---|
| $T_1$ | 2.107 eV (588 nm) | 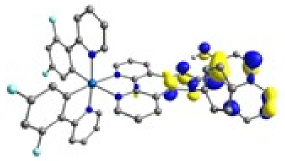 | 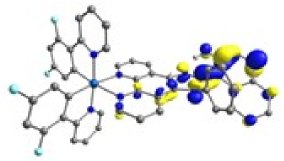 |
| $T_2$ | 2.723 eV (455 nm) | 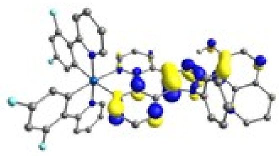 | 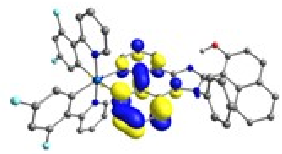 |
| $T_3$ | 2.792 eV (444 nm) | 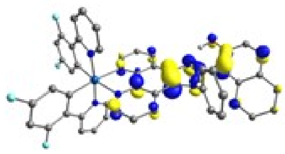 | 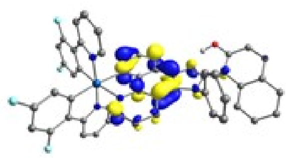 |
| $T_4$ | 3.202 eV (387 nm) | 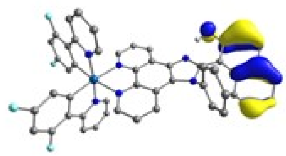 | 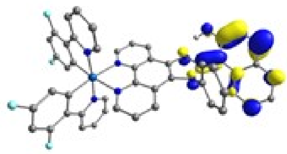 |
| $T_5$ | 3.254 eV (381 nm) | 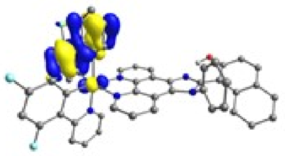 | 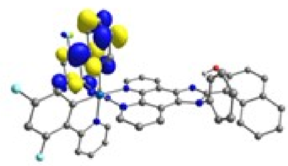 |

**Figure S11.** The highest occupied natural transition orbital (HONTO) and lowest unoccupied natural transition orbital (LUNTO) of the optimized structure of the $T_1$ state of the enol form (Ir-PIPN). The contributions of HONTO and LUNTO are more than 50 %.

| State | Energy | HONTO | LUNTO |
|---|---|---|---|
| $T_1$ | 1.915 eV (647 nm) | 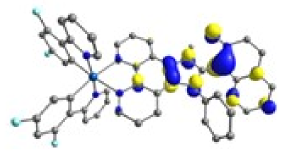 | 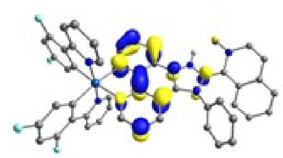 |
| $T_2$ | 2.363 eV (525 nm) | 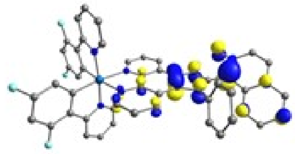 | 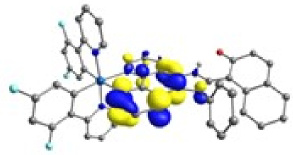 |
| $T_3$ | 2.460 eV (504 nm) | 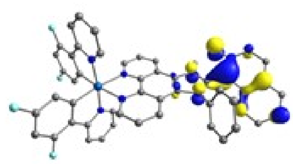 | 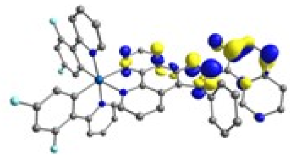 |
| $T_4$ | 3.066 eV (404 nm) | 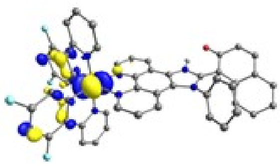 | 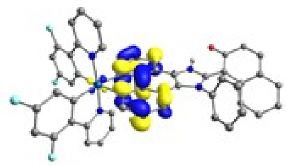 |
| $T_5$ | 3.179 eV (390 nm) | 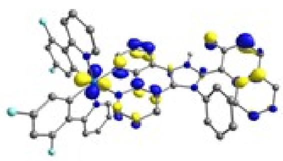 | 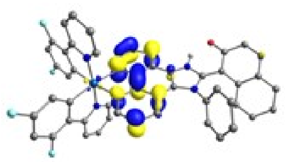 |

**Figure S12.** The highest occupied natural transition orbital (HONTO) and lowest unoccupied natural transition orbital (LUNTO) of the optimized structure of the $T_1$ state of the keto form (Ir-PIPN). The contributions of HONTO and LUNTO are more than 50 %.

| State | Energy | HONTO | LUNTO |
| --- | --- | --- | --- |
| $T_1$ | 2.409 eV (515 nm) | 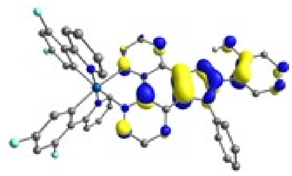 | 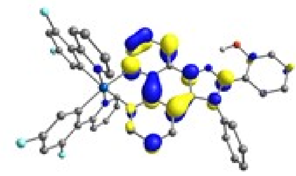 |
| $T_2$ | 2.827 eV (439 nm) | 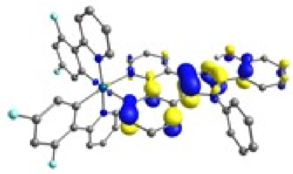 | 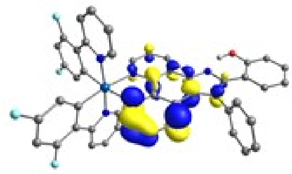 |
| $T_3$ | 3.095 eV (401 nm) | 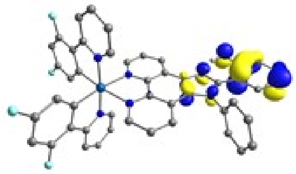 | 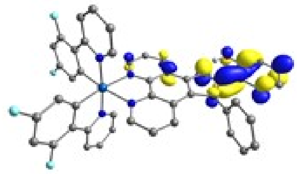 |
| $T_4$ | 3.221 eV (385 nm) | 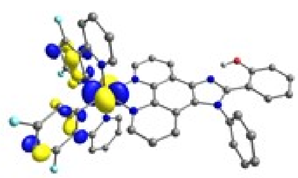 | 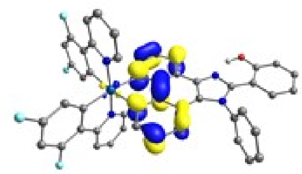 |
| $T_5$ | 3.262 eV (380 nm) | 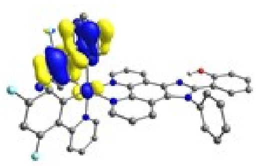 | 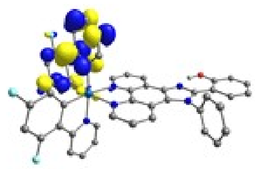 |

**Figure S13.** The highest occupied natural transition orbital (HONTO) and lowest unoccupied natural transition orbital (LUNTO) of the optimized structure of $T_1$ state of the enol form (Ir-PIPP-H). The contributions of HONTO and LUNTO are more than 40 %.

| State | Energy | HONTO | LUNTO |
|---|---|---|---|
| $T_1$ | 1.798 eV (690 nm) | 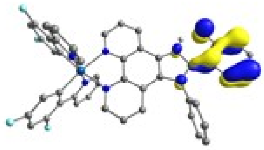 | 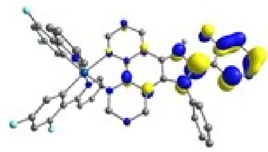 |
| $T_2$ | 2.363 eV (525 nm) | 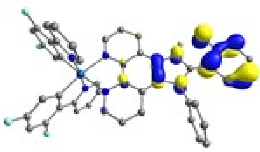 | 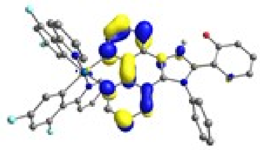 |
| $T_3$ | 2.422 eV (512 nm) | 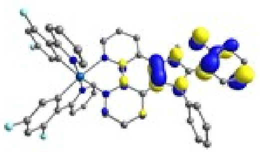 | 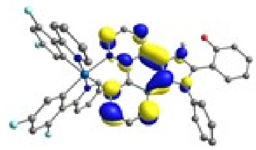 |
| $T_4$ | 3.247 eV (382 nm) | 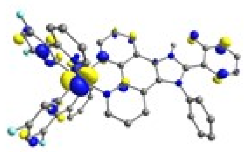 | 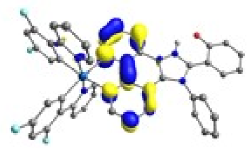 |
| $T_5$ | 3.257 eV (381 nm) | 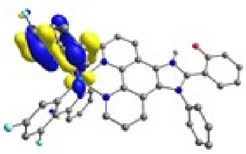 | 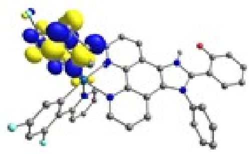 |

**Figure S14.** The highest occupied natural transition orbital (HONTO) and lowest unoccupied natural transition orbital (LUNTO) of the optimized structure of $T_1$ state of the keto form (Ir-PIPP-H). The contributions of HONTO and LUNTO are more than 40 %.

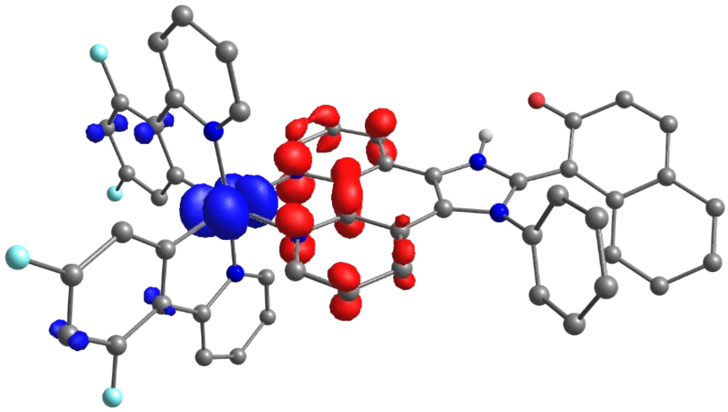

**Figure S15.** Charge density difference (CDD) of Ir-PIPN. The CDD plot shows the change in the charge distribution induced by the MLCT transition of the keto form. The blue and red densities indicate the decrease ($\boldsymbol{\delta}^{+}$) and increase ($\boldsymbol{\delta}^{-}$) of negative charge densities, respectively.

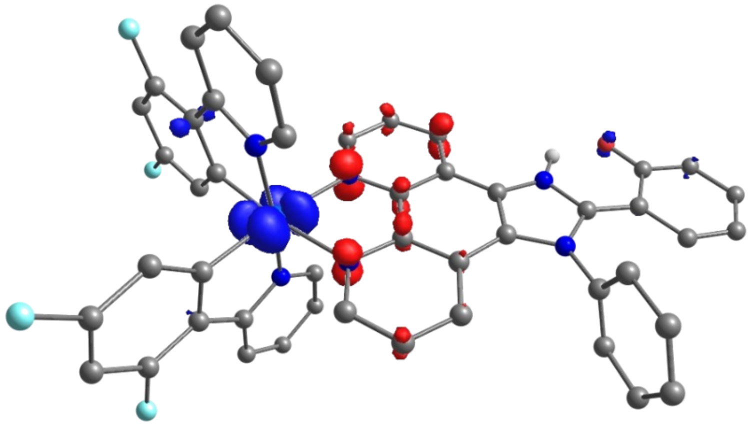

**Figure S16.** Charge density difference (CDD) of Ir-PIPP-H. The CDD plot shows the change in the charge distribution induced by the MLCT transition of the keto form. The blue and red densities indicate the decrease ($\boldsymbol{\delta}^{+}$) and increase ($\boldsymbol{\delta}^{-}$) of negative charge densities, respectively.

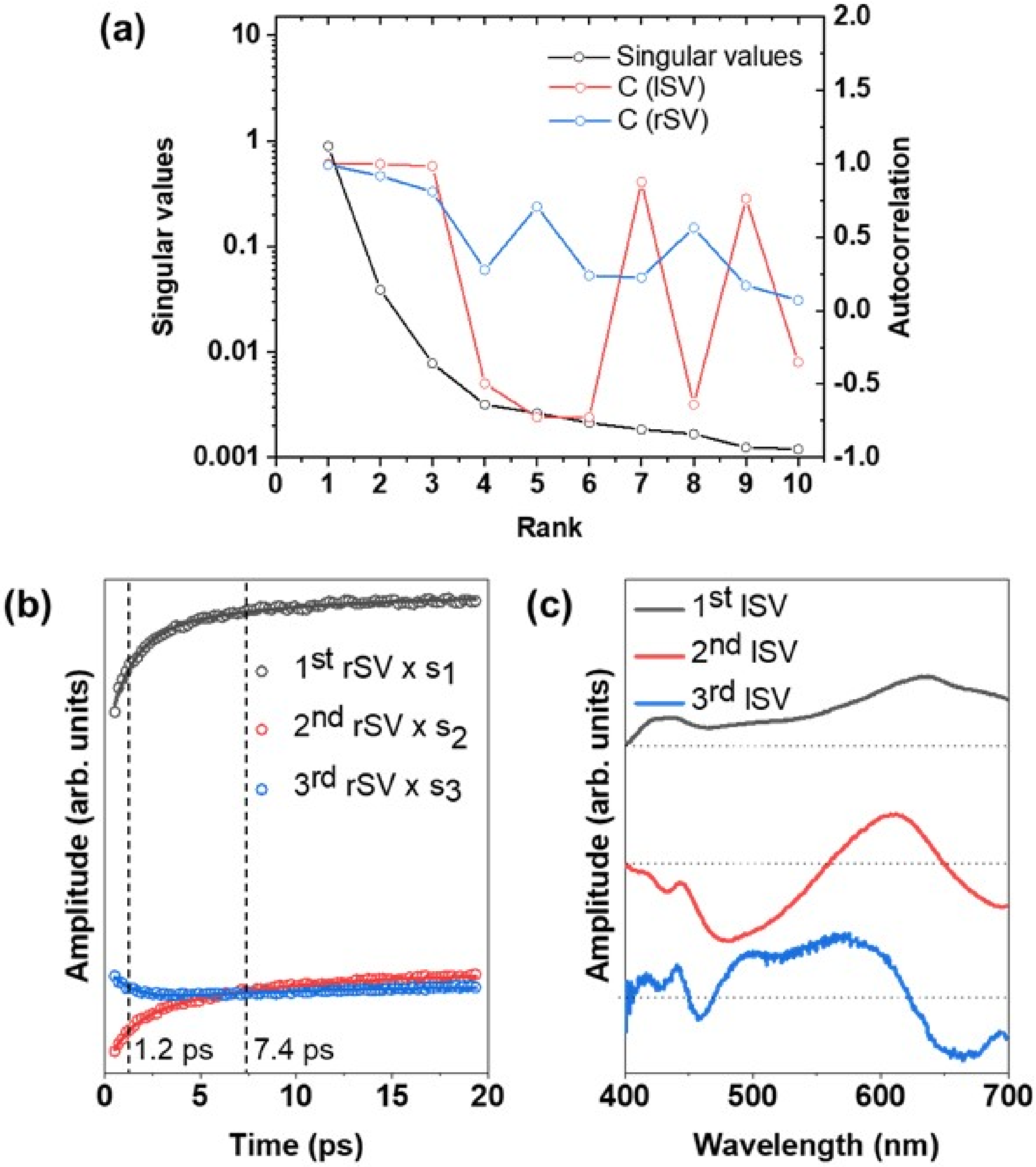


**Figure S17.** (a) The SVD results of Ir-PIPN in the DCM/EtOH (20/80) mixture. The singular values and the autocorrelation values for left singular vectors (lSVs) and right singular vectors (rSVs) obtained from SVD analysis of TA experimental data of Ir-PIPN in DCM/EtOH (20/80). The singular values and the autocorrelation values indicate that up to three components contribute significantly to the TA data. (b) The first three rSVs weighted by the corresponding singular values. The solid lines are the fits by the sum of exponential functions sharing two time constants of 1.2 ± 0.1 ps and 7.4 ± 0.5 ps. (c) The first three lSVs.

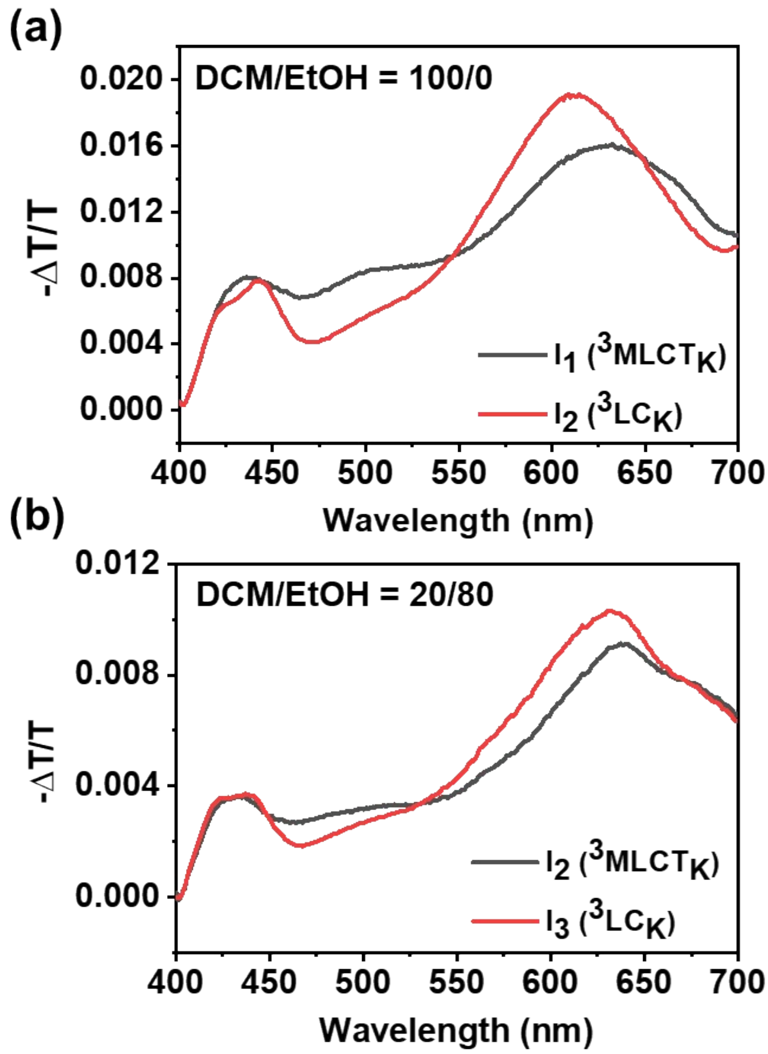


**Figure S18.** Species-associated difference spectra (SADS) corresponding to $^3MLCT_K$ and $^3LC_K$ of (a) Ir-PIPN in DCM and (b) in Ir-PIPN in DCM/EtOH (20/80). The spectral features of $^3MLCT_K$ and $^3LC_K$ and their relative difference are similar regardless of the solvent.

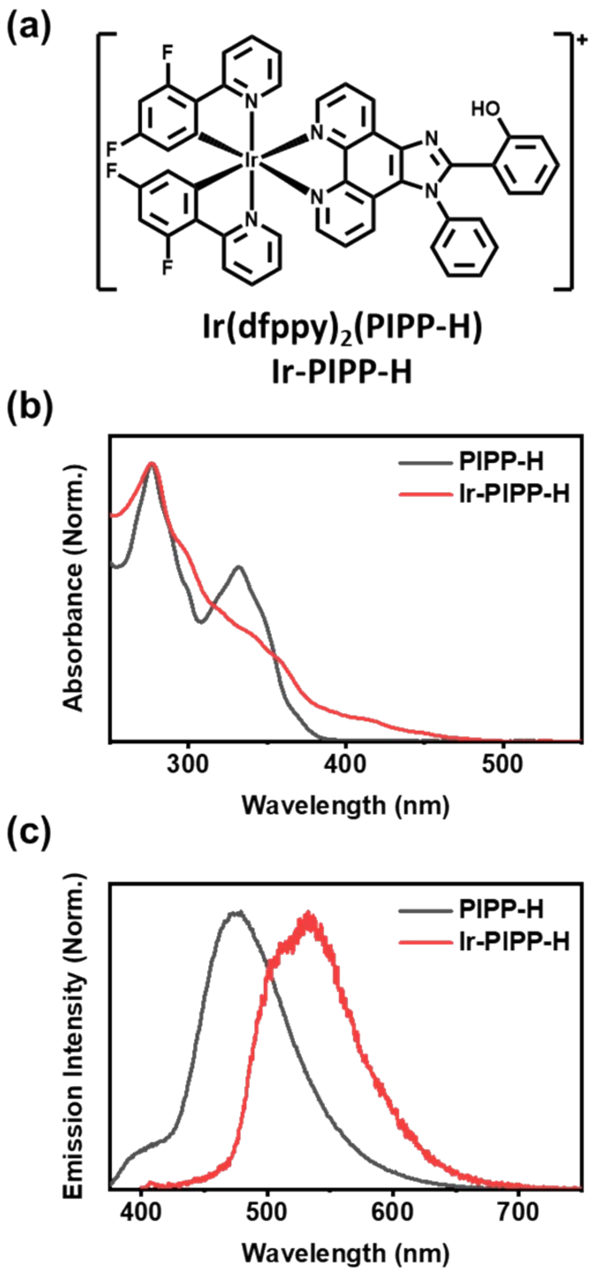


**Figure S19.** (a) Molecular structure of Ir-PIPP-H. (b) Normalized steady-state absorption spectra of the free PIPP-H ligand and Ir-PIPP-H in DCM. (c) Normalized steady-state emission spectra of the free PIPN ligand and Ir-PIPN in DCM with the 350 nm and 365 nm excitation, respectively.

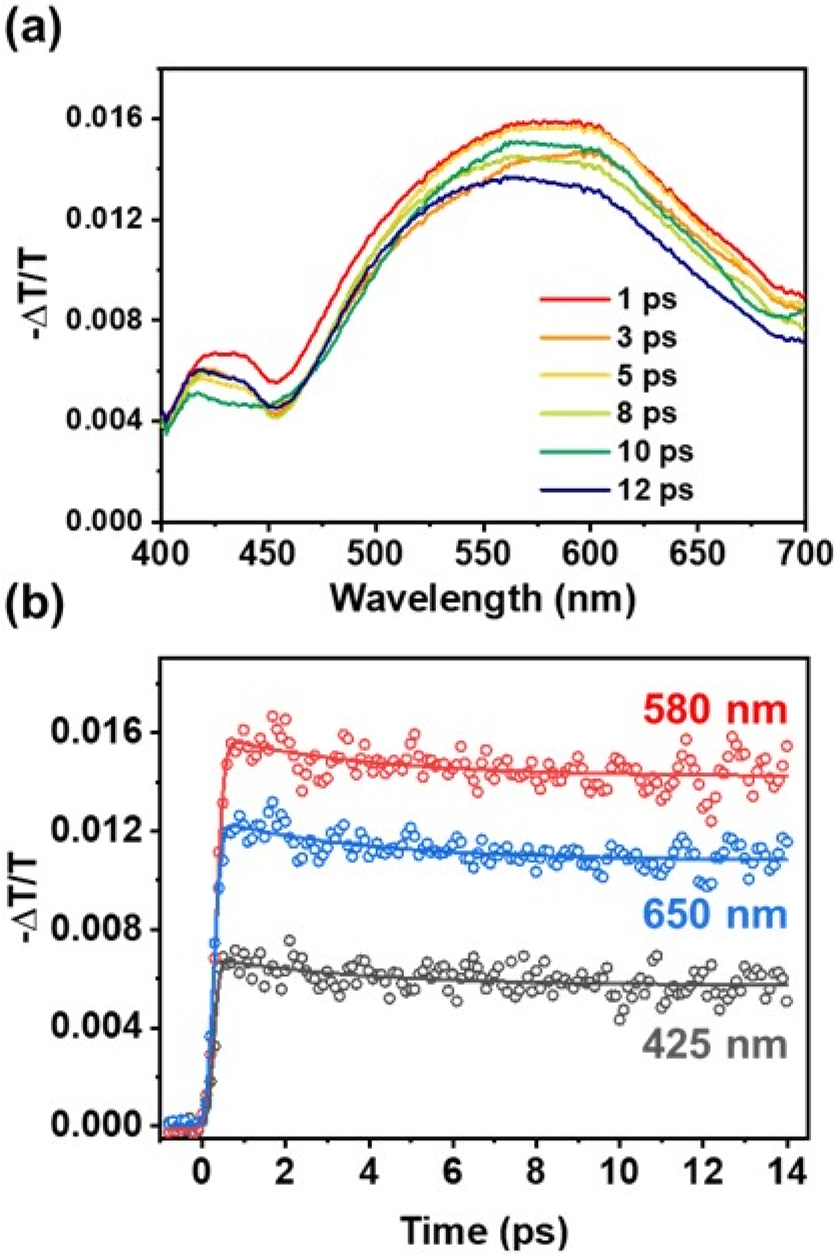


**Figure S20.** (a) TA spectra of Ir-PIPP-H in DCM at representative time delays. The excitation wavelength is 350 nm. (b) Time profiles monitored at three different wavelengths.